Nanostructure and interfacial mechanical properties of PEG/cellulose nanocomposites studied with molecular dynamics

Wenqiang Liu, Ali Shomali, Chi Zhang, Benoit Coasne, Jan Carmeliet, Dominique Derome

Nanostructure and Interfacial Mechanical Properties of PEG/Cellulose Nanocomposites Studied with Molecular Dynamics

Wenqiang Liu[1], Ali Shomali[2], Chi Zhang[2], Benoit Coasne[3], Jan Carmeliet[2] and Dominique Derome[1]

[1] *Department of Civil and Building Engineering, Université de Sherbrooke, Sherbrooke, Canada*
[2] *Chair of Building Physics, Department of Mechanical and Process Engineering, ETH Zurich, 8093, Zurich, Switzerland*
[3] *Univ. Grenoble Alpes, CNRS, LIPhy, 38000 Grenoble, France*

Abstract

Polyethylene glycol (PEG) is used to treat wood as a consolidation method. The effect of PEG on the shear strength during pull-out of crystalline cellulose (CC) fiber out of an amorphous cellulose matrix is simulated with molecular dynamics. The interfacial shear force shows a stick-slip behavior and is weakened with increasing moisture content. The shear strength increases at low moisture content, manifesting a slight strengthening of interfacial mechanical property due to cohesive forces exerted by the water molecules. At higher moisture content the shear strength reduces due to breakage of the hydrogen bonds between CC and matrix by water molecules. When adding PEG, amorphous cellulose around the crystalline fiber is replaced by PEG, forming a mixture with the amorphous cellulose. It is found that PEG-treated CC-AC composite maintains its shear strength and does not deteriorate the dependence of the shear strength on moisture content. A shear strength model based on the number of hydrogen bonds between the fiber and the matrix is developed and validated. The model reveals that, although the shear strength per hydrogen bond between the fiber and PEG is lower than the shear strength per hydrogen bond between the fiber and amorphous cellulose, the final shear strength is partly compensated by an increase in the total number of hydrogen bonds with increasing PEG ratio. Since PEG reduces the moisture content in the composite at low relative humidity, PEG treated wood in museum conditions (RH<40%) will show enhanced shear strength. The framework is a basis for further investigation of realistic archeological wood with PEG-treatment.

Keywords: Shear strength; Polyethylene glycol; Composite; Stick-slip; Molecular dynamics simulation

1. Introduction

Wood plays a significant role in human history, from the Neolithic period to modern times [1]. Because of its abundance, biocompatibility, and versatility, wood has a long history of being used in various fields, such as for fuels, construction, tools, and paper fabrication. Wood

has a multiscale hierarchical structure consisting of lumber, growth ring, cell, and layered cell wall material [2]. At the cell wall level, the cell wall has a layered structure and is composed of multiple components, within which the S2 layer is the thickest and plays a key role in the wood cell wall's mechanical properties. The S2 layer can be considered as a biopolymer composite material as it is composed of stiff crystalline cellulose (CC) microfibrils embedded in a soft matrix of hemicellulose and lignin.

Since cellulose-based composites possess abundant hydroxyl groups and show a nanoscale porosity, wood cell walls are sensitive to moisture from the ambient environment. The moisture-induced deformation upon hydration/dehydration of the wood cell walls is at the origin of wood swelling/shrinkage at the macroscopic scale. With the adsorption of water molecules, the hydrogen bonds between the wood polymers are broken and replaced by water-polymers hydrogen bonds which leads to mechanical weakening. With the help of molecular dynamics (MD) simulation studies, the predominant role of hydrogen bonds between polymer-polymer and water-polymers during hydration can be revealed [3].

Polyethylene glycol (PEG) is one of the most commonly used consolidants to treat decayed archeological wood artifacts such as the shipwrecks Mary Rose and Vasa [4,5]. Studies show that PEG-treatment provides an increased dimensional stability and reduced shrinkage of wood during drying, replacing water by PEG in the pore space. The PEG treatment may also lead to a weakening of wood mechanical properties [4], such as lower stiffness, indentation hardness, and higher creep deformation in comparison with untreated wood [8]. Although PEG has been used for decades to treat archaeological wood, the structure of wood cell wall at the molecular level after PEG treatment, the corresponding mechanical properties as well as the fundamental mechanism underneath the consolidation still need to be elucidated.

The sorption-induced phenomena observed at the macroscopic scale are determined by the interactions of water molecules and the wood cell wall at microscopic scale. However, due to the limitations of contemporary experimental techniques, a full understanding of the water-polymer interactions and induced cell wall structure modification at the atomistic scale is a formidable task without advanced computational modeling methodology. In recent years, MD simulation has been used in many woods cell wall-related studies. Due to its ultrahigh temporal-spatial resolution, atomistic-level details can be obtained, leading to a better understanding of the fundamental mechanisms for anisotropic swelling, and mechanical weakening of the woods cell wall upon hydration. MD study of a cellulose fiber-reinforced composite reveals its fundamental feature of hygromechanical behavior over the full hydration range [9]. In [9], anisotropic swelling and the interphase region generated by the fiber reinforcement, and the stick-slip behavior revealed by pullout test were documented. The decisive role of interface interaction and hydrogen bonds on the slick-slip behavior was illustrated. The study

demonstrated the capacity of MD to investigate the hygro-mechanical behavior of wood cell wall at the molecular scale and unraveled the underlying mechanism of hygro-mechanical properties determined by water-polymer interaction.

In the present study, a representation of a simplified model of wood S2 cell wall layer with PEG-treatment is established by using a composite composed of crystalline cellulose (CC) incorporated in PEG-treated amorphous cellulose (AC) matrix. The inspiration of the system studied in this work is from our previous research of the all-cellulose composites [10], which maintains the key sorption and mechanical properties of fiber-reinforced composites and circumvent the difficulty of realizing a realistic chemical structure of decayed archaeological wood. The shear strength during pull-out is examined for different PEG ratios with MD simulation. First, properties of the composites at the nanoscale are investigated. The atom number density profiles of AC and PEG in the composites influenced by the fiber-matrix interface interaction for different hydration levels is probed. The swelling of the composite, and the hydrogen bond network at the interface for different PEG ratios and moisture contents are studied. Then, the impact of PEG treatment on the interfacial mechanical properties of the composites are investigated by pullout tests. Furthermore, based on an extensive MD dataset, a shear strength model is developed assuming that the shear stress is proportional to the hydrogen bond density between the crystalline fiber and the amorphous matrix. The analysis supported by the model provides an understanding of the mechanism of the impact of PEG treatment on interfacial mechanical properties at molecular level. Finally, conclusions and suggestions for future research are drawn.

2. Materials and methods

2.1. MD settings

MD simulations are carried out using GROMACS package version 2018.8 [11]. Newton's equation of motion is integrated with the leap-frog algorithm and the time step for the integration is 1 fs. For thermostat coupling, the temperature is controlled by the v-rescale scheme [12]. The pressure is controlled by the Parrinello-Rahman barostat. The cut-off radii for the calculation of Coulomb and Van der Waals forces are both 1.2 nm. The fast smooth Particle-Mesh Ewald method is used to calculate the long-range Coulomb interactions. The neighbor list is enumerated based on the Verlet cutoff scheme every 10 timesteps. The interaction between the atoms of polymers is described by the OPLS-AA force field [13] and the full parameters are obtained by utilizing the TPPMKTOP database [14]. The data collected in this study is the average value of two realizations.

2.2. Preparation of the dry composites

Wood cell wall is made of a network of stiff cellulose microfibrils embedded in a compliant polymer matrix [15]. As a simplified model of S2 layer, the composite is composed of crystalline cellulose (CC) and surrounding amorphous matrix representing one elementary fibril. Inspired by our former work we choose as model amorphous cellulose (AC) as amorphous matrix [16]. This model is based on the all-cellulose composite concept, which considers bio-composites where the matrix is a dissolved and regenerated cellulose, and the reinforcement is an undissolved or partly dissolved cellulose. PEG molecules are introduced into the AC matrix to realize the PEG-treatment of wood cell wall.

The initial configuration of CC is generated by the Cellulose-Builder toolkit [17], in which the crystalline structure of cellulose based on the crystallographic structure reported by Nishiyama et al. [18] is used. The CC consists of 36 chains in Iβ form while each chain is composed of 5 cellobiose units – as a result, the length is approximately equal to 5.3 nm. The cross-section of the CC is a hexagonal shape with dimensions of roughly 5 × 3 nm^2, which is one of the most frequently proposed configuration for the elementary fibril of the wood cell wall though various other forms have also been suggested [19–21]. The lateral dimensions of the elementary cellulose fibril in the wood secondary cell wall are several nanometers, while the longitudinal direction can be up to μm [22]. The perimeter and cross-section area of CC is calculated to be about 13 nm and 12 nm^2, respectively, with the help of the convex hull function of SciPy [23]. By multiplying length and perimeter of CC, the contact area between CC and the amorphous matrix is determined to be about 69 nm^2.

Considering the ultrahigh length-to-diameter ratio, it is reasonable to assume that CC is infinitely long along the longitudinal direction as already implemented in previous research [9,10]. To achieve this purpose, the cellobiose units at the periodic boundaries are adjusted, so that the atomic interactions are repeated similar as in the middle of the cellulose chain. The equilibration of the initial cellulose fibril is implemented by a combination of energy minimization using a conjugate-gradient algorithm, NVT at temperature T = 300 K and NPT at pressure P = 0 bar and temperature T = 300 K. The density of CC after equilibration is around 1.6 g cm^{-3}, which compares well with experimental values.

The AC matrix is composed of 25 cellulose chains with a degree of polymerization (DP) of 25 cellobiose units. PEG molecules with DP of 4 monomers, i.e., PEG200, which is the shortest PEG used in practice for the conservation of waterlogged archaeological wood [24], are used. PEG molecules are incorporated within the AC matrix with the aim to mimic the PEG-treatment. Depending on the specific mass ratio of PEG, a certain number of PEG molecules are used to build the PEG-treated composites. With the help of Packmol [25], the relaxed

structure of CC as well as randomly distributed AC chains and PEG molecules are packed into an orthogonal box with periodic boundary conditions applied in all three directions.

The initial configuration is subjected to one energy minimization step and a series of relaxation steps, which includes NVT (T = 300 K) for 1 ns, NPT (T = 300 K, P = 0 bar) for 10 ns, NPT (T = 450 K, P = 0 bar) for 10 ns, NPT (T =600 K, P = 0 bar) for 5 ns and NPT (T = 300 K, P = 0 bar) for 10 ns. To facilitate the further rearrangement of AC and PEG molecules, the structure is annealed by a combination of NVT (T = 700 K) for 10 ns, NVT (T = 500 K) for 5 ns, NVT (T = 300 K) for 5 ns, NPT (T = 300 K, P = 0 bar) for 10 ns to obtain the final structure of the dry state. The protocol for packing the composite is adapted from our prior research on amorphous cellulose [26] and all-cellulose composites [10], where the elevated temperature is applied to induce efficient relaxation of the molecular chains of the matrix. Throughout the final NPT run, the system's potential energy, volume, and density are allowed to reach equilibrium with fluctuations around a stable value. During the high-temperature relaxations, strong harmonic potentials are applied to pairwise carbon atoms of CC to maintain the ordered crystalline structure, which follows the procedure used in our previous studies [9,10]. The harmonic restraints are exclusively applied to CC and are removed during further low-temperature relaxations, thereby the influence on the dynamics of the atoms is negligible.

The PEG ratio is defined as:

$$m_{PEG} = \frac{mass_{PEG}}{mass_{AC}} \tag{1}$$

To study the effect of PEG-treatment with various levels on the structural and mechanical properties, composites with PEG ratios of 0%, 5%, 10%, 15%, 20%, 25%, and 30% are constructed.

2.3. Hydration

Moisture content is gradually increased by inserting water molecules one after another into each CC-AC-PEG composite based on a random insertion scheme. The water molecules based on the SPC model are inserted in randomly selected locations without overlapping with existing atoms, representing water molecules that are adsorbed by the amorphous matrix in the available porous region. After each successful insertion, one conjugate gradient energy minimization and one NPT relaxation (T =300 K, P = 0 bar) for 10 ps are applied consecutively to relax the system.

The moisture content is defined as the mass of water divided by the mass of the amorphous matrix, namely the mass of AC and the mass of PEG in total:

$$m = \frac{mass_{water}}{mass_{AC} + mass_{PEG}} \quad (2)$$

It should be noted that the moisture content is usually defined as the ratio of the mass of water to the mass of dry material, which means the mass of CC would be included in the dry mass as the denominator. However, since the crystalline core of CC does not adsorb water molecules only the mass of the amorphous matrix is considered in the determination of moisture content, following previous MD studies of wood cell wall composite [9,10]. The highest moisture content reached in this study is 0.3. Table S1 in appendix A1 gives the PEG ratio (m_{PEG}) and the moisture content (m) of all the composites studied.

2.4. Pullout test

Pullout tests are used to quantify the mechanical properties of the interface between crystalline fiber and amorphous matrix. The shear stress versus displacement of CC is recorded during the pullout process. A pulling force is applied at the geometrical center of CC atoms by a virtual spring with a spring constant $k_{pull} = 16.61$ J·m^{-2} moving at a constant velocity $v_{pull} = 0.1$ m·s^{-1} (See Figure 1). Limited by computational cost, the pulling speed is chosen to be a value as low as possible which allows the amorphous matrix to relax. The constant of the virtual spring and the pulling speed are carefully selected by prior test runs to ensure the occurrence of stick-slip behavior rather than steady sliding. For the atoms of amorphous matrix, the center of mass translational velocity is removed every 100 MD steps, to prevent that the matrix from drifting away.

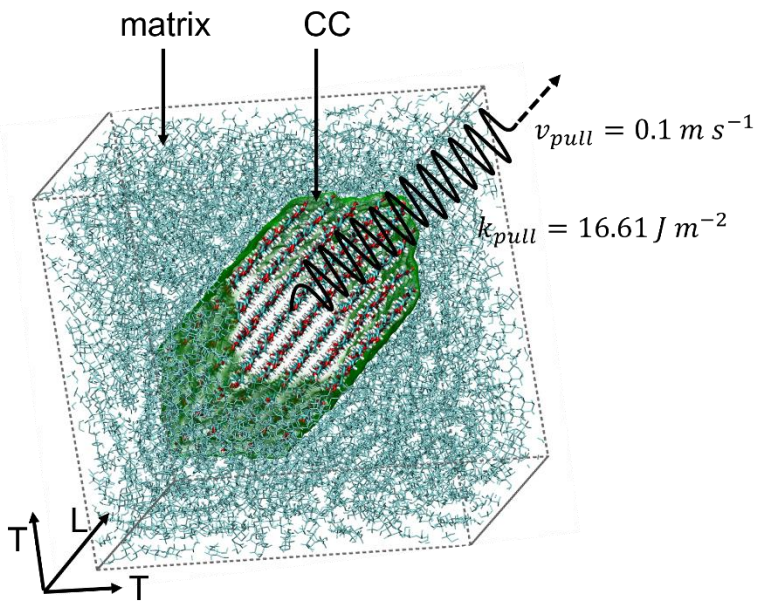

Figure 1. Schematic view of the pullout test. The crystalline cellulose (CC) fiber is embedded in an amorphous cellulose matrix. The green surface shows the boundary between CC and the matrix. The virtual spring with a spring constant of k_{pull} applies a pulling force at the geometrical center of CC and the other end of the virtual spring moves at constant velocity v_{pull}.

2.5. Measurement

2.5.1. Swelling strain

The CC is surrounded by an amorphous matrix with a thickness of about 2 nm. Although the crystalline cellulose is anisotropic due to its hexagonal-shaped cross-section, we assume the composite transversely isotropic in terms of swelling strain following our previous work [9]. This is reasonable since the difference in elastic properties between the two transverse directions is negligible when compared to the much larger stiffness in longitudinal direction [9]. The uniaxial swelling strain in the three orthogonal directions (ε_X, where X = x, y, z) is defined as:

$$\varepsilon_X = \frac{X(m) - X(0)}{X(0)} \tag{3}$$

where $X(m)$ is the size of the system at moisture content m, and $X(0)$ is the size of the system in dry condition, namely applying a Lagrangian approach. The *x* and *y* axes are the transverse

directions (T) and the z-axis the longitudinal direction (L). Two uniaxial swelling strains are determined, i.e., $\varepsilon_L = \varepsilon_z$ and $\varepsilon_T = (\varepsilon_x + \varepsilon_y)/2$. Due to the elastic modulus of crystalline nanofiber along the longitudinal direction (~150 GPa [27]) being several times higher than that in the transverse direction (18 – 50 GPa [28]), the swelling strain in the longitudinal direction is almost 0 at all moisture contents. Therefore, only swelling strain in transverse direction is reported in this work.

2.5.2. Number density of atoms

The interaction between CC and the amorphous matrix has a significant influence on the distribution of the atoms close to their interface [9]. To quantitively address this impact, the number density of atoms (ρ_N) as a function of the distance to the CC surface (d_{CC}) is determined, where ρ_N is defined as:

$$\rho_N(d_{CC}) = \frac{N(d_{CC} + \Delta d) - N(d_{CC})}{V(d_{CC} + \Delta d) - V(d_{CC})} \tag{4}$$

where $N(d_{CC})$ is the number of atoms within the distance d_{CC} to the CC surface, and $V(d_{CC})$ is the volume occupied by these atoms.

The enrichment of the atom density by the interface $\Delta\rho_N$ is defined as in our previous work [9] as the difference between the maximum value $\rho_N^{\text{peak}} = \max(\rho_N(d_{CC}))$ and the relative constant the number density ρ_N^{flat} reached sufficiently far away from the CC surface:

$$\Delta\rho_N = \rho_N^{\text{peak}} - \rho_N^{flat} \tag{5}$$

2.5.3. Displacement and shear stress during pullout

The displacement of CC at time t is defined as the distance the center of mass of CC moved from its initial position to its current location. The interface shear stress τ at time t is defined as the shear force applied to the CC fiber divided by the contact area of CC and matrix, i.e. ~69 nm^2 as noted in subsection 2.2. The maximum values of the shear force are determined as the peaks in the shear stress-displacement curve.

2.5.4. Characterization of hydrogen bond

The number of hydrogen bonds ($\#HB$) formed between CC and the amorphous matrix are determined, where a hydrogen bond (HB) is defined based on the following geometric criterion [9]:

$$r \leq 0.35 \text{ nm and } \alpha \leq 30° \quad (6)$$

where r is the distance between the donor oxygen and acceptor oxygen atom, and α is the angle determined by acceptor oxygen atom – donor oxygen atom – donor hydrogen atom. The threshold of 0.35 nm equals the first minimum of the radial distribution function of SPC water [29]. The angle of 30° is approximately the angle of vibrations that break HBs [30].

The areal density of interfacial hydrogen bonds, $\#HB\ A^{-1}$, is defined as the number of hydrogen bonds between CC and the amorphous matrix normalized by the contact area between CC and the matrix. The protocol to determine the hydrogen bond follows our previous work [9]. The local maxima in the areal density of interfacial hydrogen bond curve are determined.

3. Results and discussion

3.1. Nanostructure and properties of composites

Figure 2 shows the measured density of the CC-AC-PEG composites in the dry state for different PEG ratios. The density of the composite first slightly increases, whereafter it drops with increasing m_{PEG}. Using the density of the crystalline fiber (1.6 g cm^{-3}, the density of AC (1.4 g cm^{-3}), and the density of PEG (1.1 g cm^{-3}), the density of the composite can be predicted using the rule of mixture (RoM) [3]. The details of the calculation can be found in appendix A2. The dashed blue line in Figure 2 shows that the composite density predicted by the RoM underestimates the density for all PEG ratios. In contrast, the prediction is in good agreement for the composite without PEG ratio. This indicates that when adding PEG to the composite, the PEG is not mixed according to its volume fraction, as assumed in a classical RoM. Detailed analysis shows that when adding PEG to the composite, part of the PEG is mixed with AC, while another part fills the initial porosity of AC. A new RoM is derived taking into account this filling process of AC porosity by PEG. The dashed black line in Figure 2 shows a good agreement between the predicted densities by the new RoM and the MD densities. This filling process results in an increase of the composite density at low PEG ratio. At high PEG ratio the compsite density decreases since the density of PEG is lower than the density of AC.

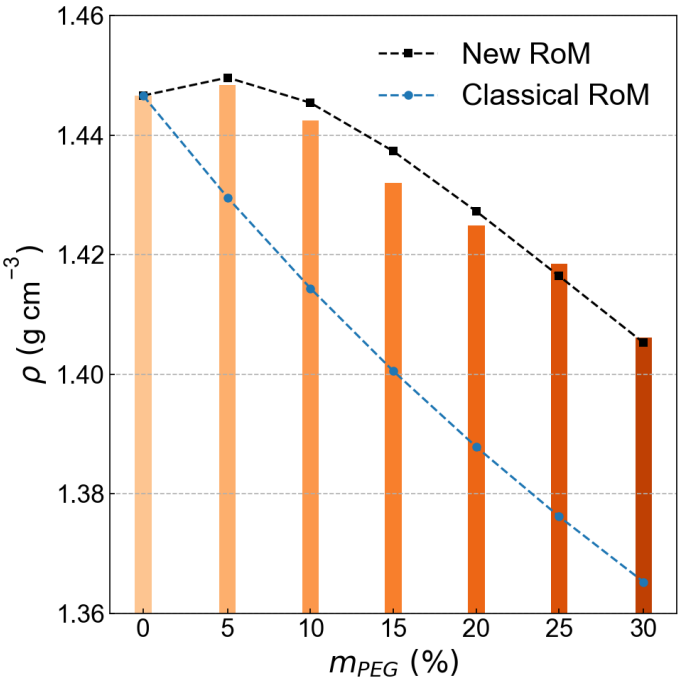

Figure 2. Density of composites at dry state as a function of PEG ratio. The blue dashed line shows the composite density predicted by the classical RoM. The black dashed line represents the composite density predicted by the new RoM, where the filling of the initial porosity of AC by PEG is considered.

The distribution of AC, PEG, and water molecules in the amorphous matrix is characterized by the atom number density profiles as a function of the distance to CC surface in Figure 3. For the dry CC-AC composite in Figure 3a, the atom number density of AC is zero close to CC and then increases rapidly to the peak values. The same observation is made for the CC_AC-PEG composite with low density for PEG at the CC interface. These results indicate a densification of AC and PEG close to the CC. Comparing Figures 3a-b shows that the peak height of AC density decreases when PEG content increases, which indicates that AC molecules are replaced by PEG molecules at the CC. The sum of the peak values of AC and PEG density increases slightly for increasing m_{PEG}, which shows that treating AC with PEG increases the total atom number density near the CC surface. However, PEG is not able to fill the total open space between CC surface and matrix. The ratio between the peak values for PEG and AC increases for increasing PEG ratio: $\rho_{N,PEG}^{peak}/\rho_{N,AC}^{peak}$ = 0.0, 0.18, 0.32, 0.42, 0.56, 0.79, 0.83 for m_{PEG} = 0, 5, 10, 15, 20, 25 and 30%, respectively. Compared to this increase in peak value ratio, the ratio between the flat values for PEG and AC increases less strongly: $\rho_{N,PEG}^{flat}/\rho_{N,AC}^{flat}$ = 0.00, 0.04, 0.09, 0.17, 0.24, 0.29, 0.39, for the corresponding m_{PEG} values, respectively. This indicates that more PEG molecules are located at CC surface than in the matrix. The location of the peak

density of PEG and AC atoms is around 0.31 nm and 0.36 nm from CC, respectively, at low moisture content (< 12 %). The peak position of AC atoms remains nearly unchanged for increasing m_{PEG}.

The atom number density profiles for water in Figures 3a-b show two distinct peaks, which are closer to CC surface in comparison to the peaks of PEG and AC. The first peak indicates that water molecules fill the open space between CC and matrix that is not accessible by PEG nor AC molecules. The second peak indicates the adsorption of water molecules by the matrix. In appendix A3, the Stokes-Einstein radius is determined for PEG chain and water molecule. The PEG diameter is found to be 3.12 Å, while for water it is 1.91 Å. This shows that the hydrodynamical diameter of PEG chain (which corresponds to the size of a carbon bead in the chain) is larger than that of water, explaining that water molecules can more easily access the open space between CC and matrix compared to PEG chains.

Figures 3c and 3d show that the peak and flat atom density values of AC and PEG decrease with increasing moisture content, while the peak and flat density values of water molecules increase substantially. The peak density values of water molecules change with increasing moisture content more significantly than the flat density values. This indicates that more water molecules are located at the CC interface than in the matrix. Comparing Figures 3c and 3d, it is found that the changes in atom number density of AC, PEG and water molecules are smaller at higher m_{PEG} (therefore, indicating less moisture sensitivity at high PEG contents). However, the strong increase in water molecules density at CC surface indicates that arrangement of water molecules around CC surface is governed mainly by the interaction between CC and water molecules.

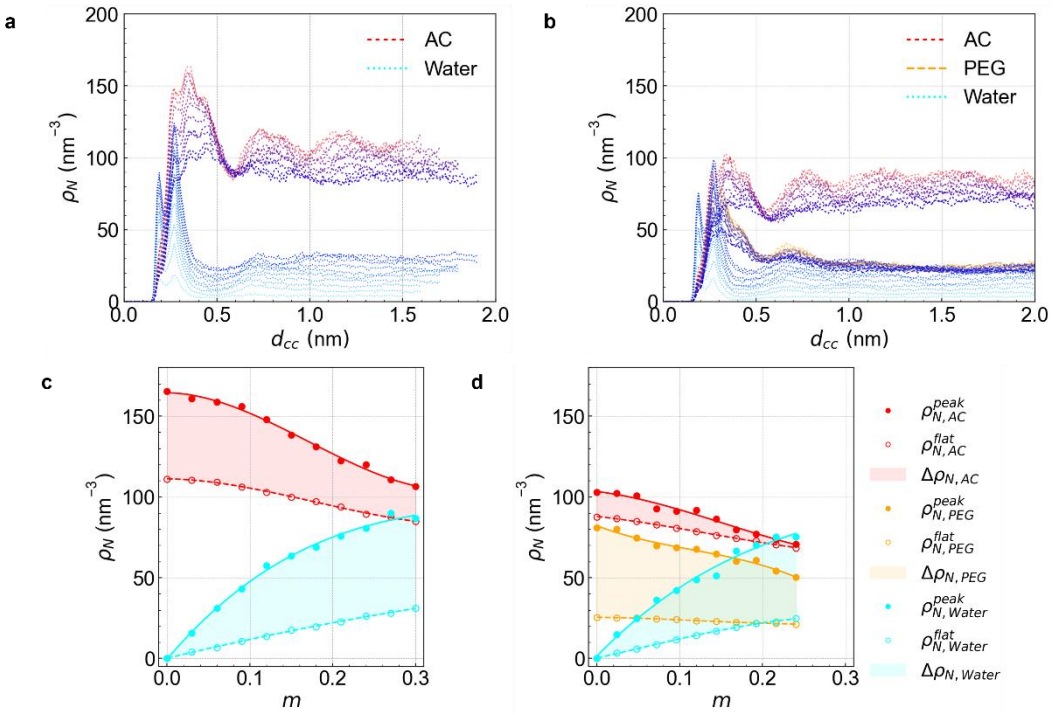

Figure 3. (a) Atom number density profiles of CC-AC as function of distance to CC surface (d_{CC}); (b) Atom number density profiles of CC-AC-PEG composite at 25% m_{PEG} as function of distance to CC surface (d_{CC}). Red, orange, and cyan dashed lines denote atom number density for AC, PEG, and water, respectively. Gradient blue lines ranging from light to dark blue overlapping with the lines in their original color correspond to 10 levels of increasing moisture content. (c) First peak and matrix flat values of atom number density for AC and water as function of moisture content for CC-AC composite. (d) First peak and matrix flat values of atom number density for AC, PEG, and water as function of moisture content for CC-AC-PEG composite at 25 % m_{PEG}.

The swelling in longitudinal direction is two or three orders of magnitude smaller than the swelling in transverse direction due to the very high stiffness of CC in longitudinal direction. Therefore, only swelling in transverse direction versus moisture content is shown in Figure 4a. The swelling curves show two regions: the curves are nonlinear at low moisture content (< 10%) while the composites swell linearly with increasing moisture content at high moisture content. Swelling coefficients are determined as the slope of the linear region of the swelling curves. Figure 4b shows that the swelling coefficients monotonically increase slightly with m_{PEG} up to 25%.

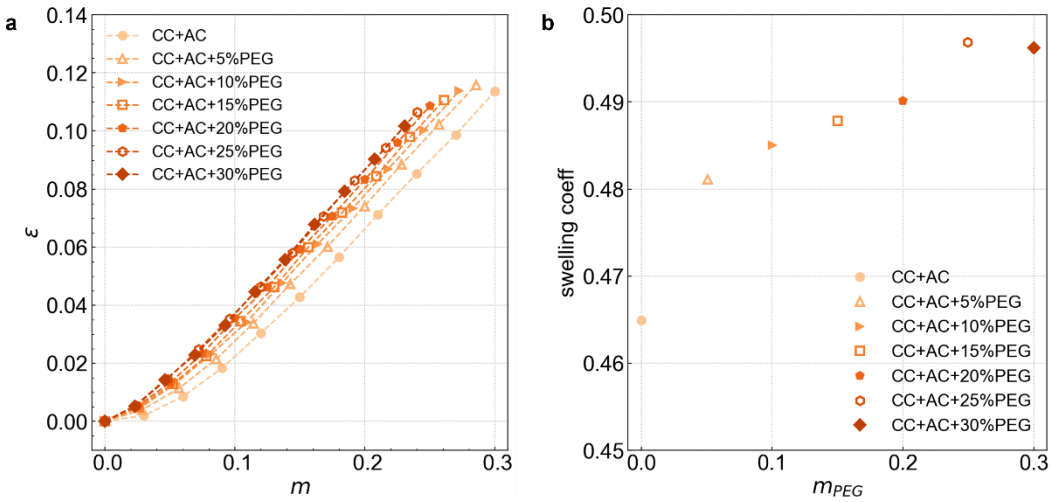

Figure 4. (a) Swelling strain versus moisture content in transverse direction for composites with different PEG ratios; (b) Swelling coefficient, which is the slope of the linear part of the swelling curve in Figure 4a, versus PEG ratio.

Figure 5a shows the areal density of interfacial hydrogen bonds ($\#HB\ A^{-1}$) between CC and AC, CC and PEG, CC and (AC+PEG) for the dry composite as a function of m_{PEG}. The areal density of hydrogen bonds (HBs) between CC and PEG increases with increasing m_{PEG}, while the areal density of HBs between CC and AC decreases. This indicates that HBs between AC and CC are broken and replaced by HBs between PEG and CC. The total areal density of HBs between CC and (AC+PEG) increases slightly, therefore indicating a slight densification due to addition of PEG at the interface. The curves in Figure 5a can be approximated by a linear relationship. A linear correlation between the number of HBs between CC and AC, and between PEG and water molecules, and the peak values of the atom number is found in Figures S2 in appendix A5. This indicates that the hydrogen bond formation between the CC, matrix and water molecules plays a major role in the atom distribution and structure of the matrix near the CC surface.

Figure 5b shows the areal density of interfacial hydrogen bonds ($\#HB\ A^{-1}$) between CC and AC, CC and water, and CC and (AC+water) for the composite without PEG as a function of moisture content. The density of HBs between CC and water increases, while the density of HBs between CC and AC decreases with increasing moisture content. Two linear regions are observed. The first region indicates the filling of the open space between CC and matrix with water molecules and the replacement of AC atoms by water molecules. The second region only represents the replacement of AC atoms by water molecules. These results are fully consistent with our interpretations above based on the density evolutions of the different systems.

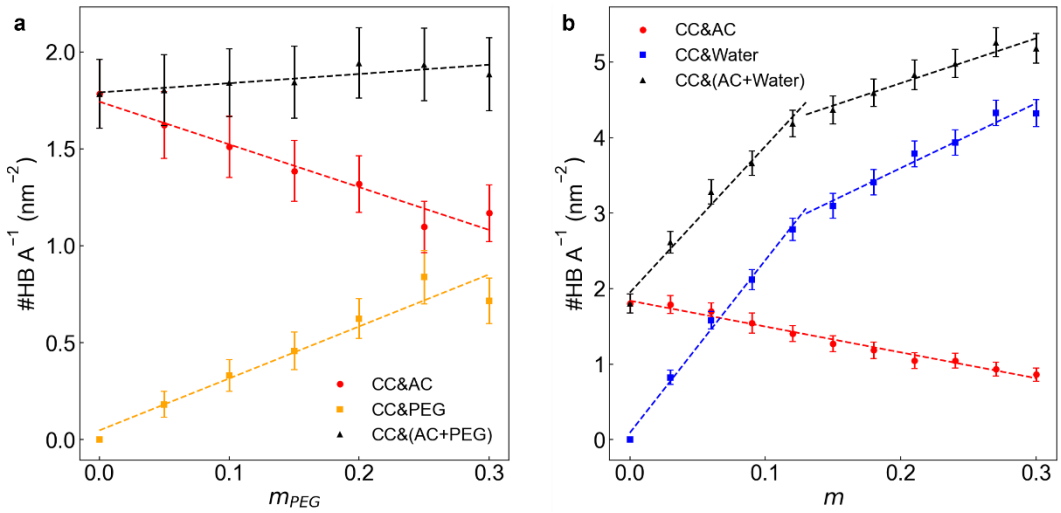

Figure 5. (a) The areal density of interfacial hydrogen bonds ($\#HB\ A^{-1}$) between CC and AC, CC and PEG, CC and (AC+PEG) versus PEG ratio for dry composites. (b) The areal density of interfacial hydrogen bonds ($\#HB\ A^{-1}$) between CC and AC, CC and water, CC and (AC+water) versus moisture content for CC-AC composite without PEG. The dashed lines show the linear least-squares fit to the data.

Figure 6a shows the areal density of interfacial hydrogen bonds ($\#HB\ A^{-1}$) between CC and (AC+PEG) versus moisture content for different PEG contents. The HB density decreases with increasing moisture content, therefore indicating that HBs between CC and AC, and CC and PEG are broken and replaced by HBs between CC and water. All data collapse onto a single curve, meaning that water molecules break the same number of HBs between CC and AC, and CC and PEG regardless of the PEG ratio. Figures 6b and 6c show the HB density between CC and AC, and CC and PEG, respectively, for different PEG ratios. The HB density decreases with increasing moisture content. The HB density between CC and AC decreases with increasing PEG ratio, while the HB density between CC and PEG increases with increasing PEG ratio. Figure 6d shows that the density of HBs between CC and water increases with moisture content and all data collapse onto a single curve for different PEG ratios. This result indicates that all composites show similar water sorption behavior at CC-matrix interface. This further shows that PEG-treatment has almost no effect on the moisture sorption behavior at the CC-matrix interface.

From Figures 6b-c, we can determine the HB densities between CC and AC, and CC and PEG that are broken during water sorption (HB density at moisture content m is subtracted from HB density at dry state). When subtracting this sum of these broken HB densities from the total HB density between CC and water in Figure 6d, we obtain the HB density of sorption sites on CC that are not occupied in the dry CC-AC-PEG composite but become occupied by

water with increasing hydration (red line in Figure 6d). This means that AC and PEG in the dry mixture only occupy a relatively small part of the available sorption sites on CC, while water can occupy these free sites which are not occupied by PEG and AC. This means that a large proportion of the available hydroxyl groups of CC are not occupied by AC and PEG and that the hydrogen bond formation between CC and water is mainly determined by the interaction between CC and water molecules. This explains why the PEG-treatment does not have an impact on the HB density between CC and water.

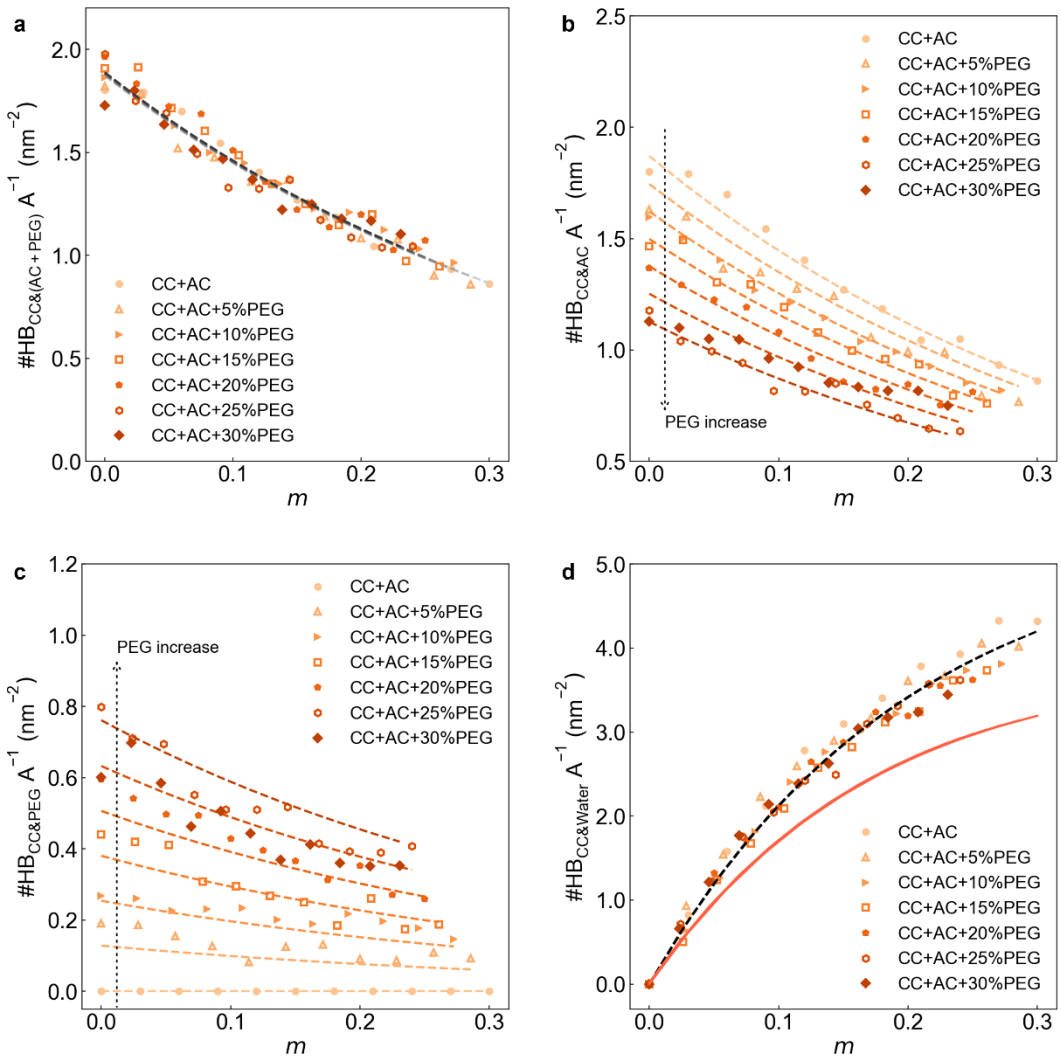

Figure 6. (a) The areal density of interfacial hydrogen bonds ($\#HB\ A^{-1}$) between CC and matrix (AC+PEG) as a function of the moisture content (m) for different PEG ratios. The dashed gray lines show the curves according to Equation 8; (b) The areal density of interfacial hydrogen bonds ($\#HB\ A^{-1}$) between CC and AC versus moisture content for different PEG ratios. The dashed lines show the curves according to Equation 9a; (c) The areal density of interfacial hydrogen bonds between CC and PEG versus moisture content for different PEG ratios. The dashed lines show the curves according to Equation 9b. (d) Density of HBs between CC and water as function of moisture content for different PEG ratios. The black dashed line is the curve according to Equation 10. The red line represents the HB density of sorption sites on CC that are not occupied in the dry CC-AC-PEG composite but becomes occupied by water molecules with increasing moisture content.

3.2. Pullout simulation

The shear stress curves versus displacement show a clear stick-slip pattern for the dry composites in Figures 7a-b (orange curves for 0% m_{PEG} and red for 25% m_{PEG}). In the stick phase, the shear stress rapidly increases over a small displacement. When the shear stress exceeds the maximum shear stress or shear strength, the CC slips and the shear stress drops rapidly with increasing displacement. The areal density of hydrogen bonds between CC and AC and between CC and AC+25%PEG mixture exhibits a similar stick-slip pattern in Figures 7c-d, respectively. This result indicates a strong correlation between shear stress and HB density. The peaks in HB density are located at the same displacement as peaks in shear stress. This indicates that the shear stress and shear strength are strongly governed by the interfacial hydrogen bond networks between CC and the matrix.

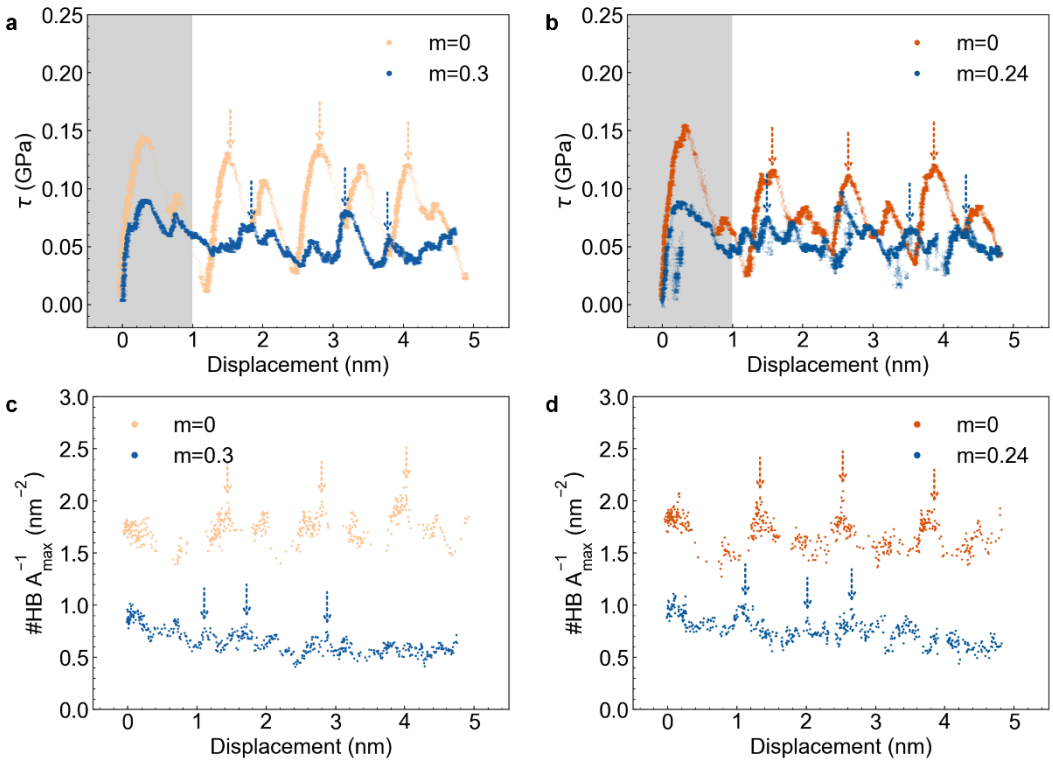

Figure 7. (a) Shear stress as a function of displacement for CC-AC composite without PEG; The light orange and blue curve correspond to moisture content of 0 and 0.3, respectively. (b) Shear stress as a function of displacement for composite with 25% PEG. The red and blue curves correspond to moisture contents of 0 and 0.24, respectively. The gray shaded region denotes the first cycle which is ignored when the peak values are extracted. The arrows point at the peak position of the maximum shear force. (c) Areal density of hydrogen bonds between CC and the matrix during the pulling out CC-AC composite without PEG; (d) Areal density of hydrogen bonds between CC and the matrix during the pulling out of CC-AC-PEG composite with 25% PEG.

Figure 8a shows a surface plot of the shear strength, defined as the mean peak shear stress τ_{max} as a function of moisture content and PEG ratio. The areal density of hydrogen bonds between CC and (AC+PEG) is shown in Figure 8b. Comparison of Figures 8a and 8b indicates a strong correlation between the shear strength and HB density over the full range of PEG ratio and moisture content. In the dry state, i.e., along the m_{PEG} axis, the shear strength increases slightly with the PEG ratio for m_{PEG} smaller than 20%. The increase in shear strength is around 10% compared with the value for the dry composite without PEG. This increase in shear strength can be attributed to the increase in total HB density with increasing PEG ratio (see Figure 5). The latter increase is caused by the densification at CC surface as indicated by the increase in the total atom number density at the interface between CC and matrix (see Figure

3). A small increase in shear strength can be observed at the moisture content of 3% due to water molecules filling the open space between CC and matrix, which leads to more cohesive interactions between CC and the matrix [9].

For moisture contents between 3% and 6% and PEG ratios between 5% to 15%, the shear strength increases compared with the value of composite without PEG at the dry state. This result indicates an enhancement of the shear strength by PEG treatment. The highest shear strength is found around 10% PEG ratio and 3% moisture content. At moisture contents above 6%, the shear strength decreases due to the breakage of the hydrogen bonds between CC and matrix. For the dry composite, the lowest shear strength is found at around 25% PEG ratio, while the total HB density does not show this decrease. Figure S3b in appendix A6 shows a local maximum of the HB density between CC and PEG at the same location, while Figure S3a shows a local minimum in HB density between CC and AC. The sum of the HB densities between (1) CC and AC and (2) CC and PEG remains however, constant. This observation implies that the shear stress provided per hydrogen bond is lower between CC and PEG than between CC and AC, which aligns with the analysis of the shear strength in Section 4.2.

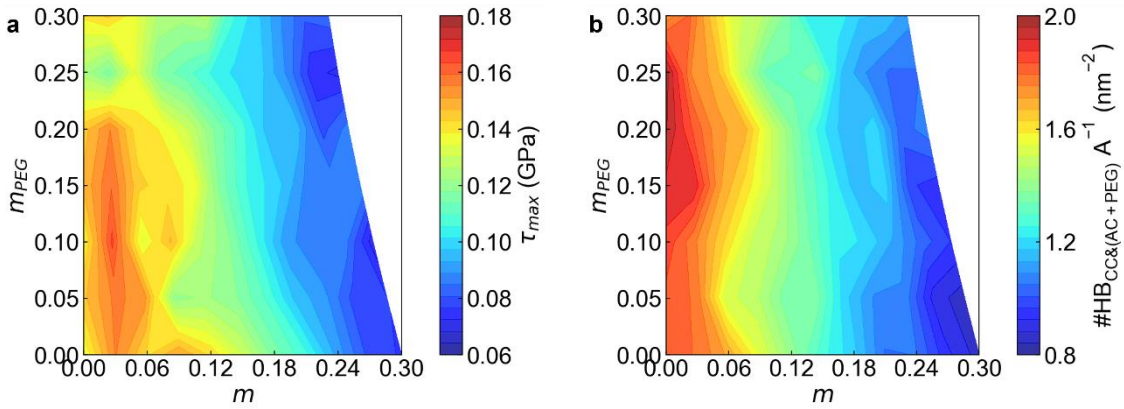

Figure 8. (a) Contour view plot of the maximum shear stress τ_{max} versus moisture content and PEG ratio; (b) Contour view plot of the areal density of hydrogen bonds between CC and (AC+PEG) versus moisture content and PEG ratio.

Figure 9a shows the relation between shear strength (maximum shear stress τ_{max}) and the areal density of interfacial hydrogen bonds between CC and AC for the composite without PEG for different moisture contents. At moisture contents lower than 9%, the shear strength is maximal and shows a plateau value $\tau_{plateau}$. In [9], we found that the shear strength equals the shear strength of the matrix, which indicates that the value is limited by the shear strength of the matrix although the shear strength between CC and matrix interface may be higher. With increasing moisture content, the shear strength τ_{max} reduces since the HB density between CC

and AC decreases due to the breakage of hydrogen bonds between CC and AC, and the replacement by hydrogen bonds between CC and water.

Figure 9b shows the results of shear stress τ_{max} versus the areal density of interfacial hydrogen bonds between CC and (AC+PEG) for all composites. The rather high scatter in the measurements of shear strength can be attributed to the variability in hydrogen bonding between CC and matrix during pullout.

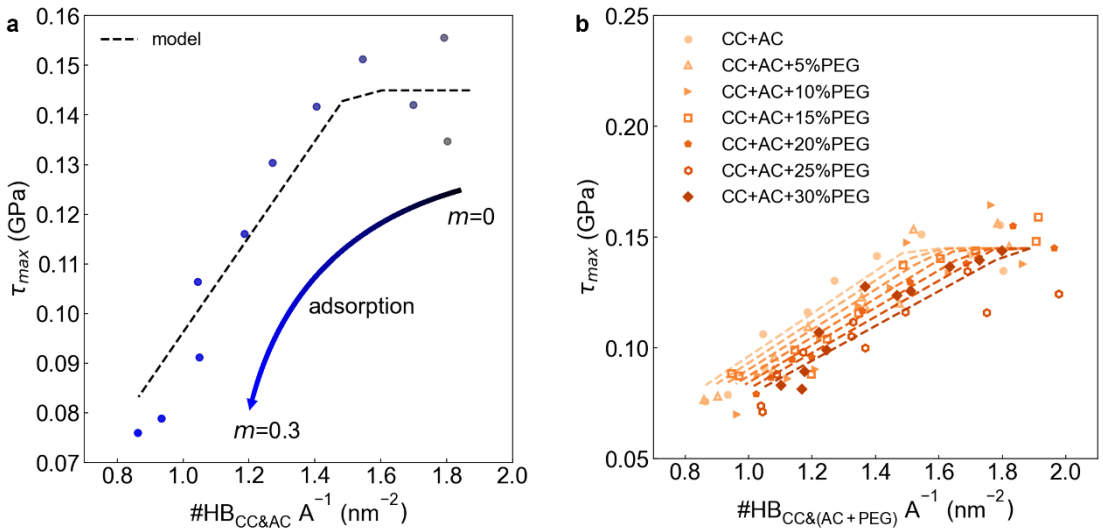

Figure 9. (a) Relation between shear strength τ_{max} and the areal density of interfacial hydrogen bonds between CC and AC for the composite without PEG for moisture contents from 0 to 0.3. The gradient blue color of the MD data points indicates the different moisture contents with the highest moisture content in dark blue. The black dashed line represents Equation 11; (b) Relation between shear strength τ_{max} and the areal density of interfacial hydrogen bonds between CC and (AC+PEG) for different PEG ratios. The dashed lines present Equation 12 of the shear strength model.

4. Model for shear strength dependent on HB density

4.1. Model for density of hydrogen bonds

Figure 5a shows a linear relation between the density of HBs between CC and AC, CC and PEG, and CC and (AC+PEG) versus PEG content for dry composites. The HB density between CC and AC, CC and PEG, CC and (AC+PEG) for the dry composite as function of the PEG ratio can then be expressed as:

$$\#HB_{CC\&AC}\, A^{-1}(dry) = a_{AC} - b_{AC} \cdot m_{PEG} \qquad (7a)$$

$$\#HB_{CC\&PEG}\ A^{-1}(dry) = b_{PEG} \cdot m_{PEG} \quad (7b)$$

$$\#HB_{CC\&(AC+PEG)}\ A^{-1}(dry) = a_{AC} + (b_{PEG} - b_{AC}) \cdot m_{PEG} \quad (7c)$$

where the coefficients a_{AC}, b_{AC} and b_{PEG} are obtained by least-square linear fitting (see Table 1). Since b_{PEG} is slightly larger than b_{AC} in Equation 7c, the total density of hydrogen bonds between CC and matrix increases slightly when PEG is added.

The dependence of the density of HBs on moisture content as shown in Figure 6a is approximated by an exponential function. The exponential decay of HB density with moisture content can be rationalized by considering that the number of HBs depends on the breakage of HBS due to water molecules (or the number of HBS depend on the number of adsorbed water molecules) and the current number of HBs. The derivation of the exponential relation is given in appendix A4. The dependence of density of HBs on PEG ratio (m_{PEG}) and moisture content (m) is then expressed as:

$$\#HB_{CC\&(AC+PEG)}\ A^{-1}(m_{PEG}, m) = [a_{AC} + (b_{PEG} - b_{AC}) \cdot m_{PEG}] \cdot \exp(-b_{MC}\ \cdot\ m) \quad (8)$$

It is worth noting that b_{MC} is found to be independent of the PEG ratio showing that water molecules break the same number of hydrogen bonds between (1) CC and AC and (2) CC and PEG. b_{MC} is obtained by fitting Equation 8 to the MD data and its value is listed in Table 1. The density of HBs between CC and AC, and CC and PEG then becomes:

$$\#HB_{CC\&AC}\ A^{-1}(m_{PEG}, m) = [a_{AC} - b_{AC} \cdot m_{PEG}] \cdot \exp(-b_{MC} \cdot m) \quad (9a)$$

$$\#HB_{CC\&PEG}\ A^{-1}(m_{PEG}, m) = [b_{PEG} \cdot m_{PEG}] \cdot \exp(-b_{MC} \cdot m) \quad (9b)$$

Using the obtained values for a_{AC}, b_{AC}, b_{PEG} and b_{MC}, the density of HBs between CC and AC, and CC and PEG are plotted in Figures 6b-c. A good agreement is obtained with the MD data.

The HB density between CC and water dependent on moisture content is modeled by a normalized exponential function:

$$\#HB_{CC\&Water}\ A^{-1}(m) = c_{MC} \frac{[1 - \exp(-d_{MC} \cdot m)]}{[1 - \exp(-d_{MC} \cdot m_{max})]} \quad (10)$$

where m_{max} is the maximum moisture content equal to 0.3. The values for c_{MC} and d_{MC} are obtained by fitting Equation 10 to the MD data in Figure 6d.

4.2. Shear strength model

Figure 9a shows a linear relation of the shear strength versus HB density until it reaches a plateau value $\tau_{plateau}$:

$$\tau_{max} = \begin{cases} \alpha_{AC} \cdot \#HB_{CC\&AC}\, A^{-1}(m), & \tau_{max} < \tau_{plateau} \\ \tau_{plateau}, & \tau_{max} \geq \tau_{plateau} \end{cases} \quad (11)$$

where $\#HB_{CC\&AC}\, A^{-1}(m_{PEG}, m)$ is given by Equation 9a for $m_{PEG} = 0$. The parameters α_{AC} and $\tau_{plateau}$ are obtained by fitting the MD data in Figure 9a. The parameter α_{AC} can be interpreted as the shear strength of a hydrogen bond between CC and AC.

Analogously, the shear strength τ_{max} of CC-AC-PEG composite depends on the HB densities between CC and AC, and CC and PEG, or:

$$\tau_{max} = \begin{cases} \alpha_{AC} \cdot \#HB_{CC\&AC}\, A^{-1}(m_{PEG}, m) + \alpha_{PEG} \cdot \#HB_{CC\&PEG}\, A^{-1}(m_{PEG}, m), & \tau_{max} < \tau_{plateau} \\ \tau_{plateau}, & \tau_{max} \geq \tau_{plateau} \end{cases} \quad (12)$$

where $\#HB_{CC\&AC}\, A^{-1}(m_{PEG}, m)$ and $\#HB_{CC\&PEG}\, A^{-1}(m_{PEG}, m)$ are given by Equations 9a and 9b, respectively. The only unknown parameter is α_{PEG} which can be interpreted as the shear strength of a hydrogen bond between CC and PEG, is determined by fitting the MD data in Figure 9b, showing a reasonable agreement. Note that we assume that the plateau value $\tau_{plateau}$ does not depend on the PEG ratio, which appears as a justified assumption considering the scatter in the MD data.

We find that $\alpha_{PEG} < \alpha_{AC}$ (see Table 1) meaning the shear force per hydrogen bond is lower between CC and PEG than between CC and AC. However, as we found in Figure 5a, the total HB density increases with PEG ratio at dry state as shown in Figure 5a. This means that the higher HB density between CC and PEG partly compensates for the lower shear force per hydrogen bond between CC and PEG. As a result, the shear strength versus total HB density in Figure 9b show similar curves, i.e. showing a plateau at the low moisture content region and linearly decreasing relation with increasing moisture content. Figure 10 shows the separate contribution of the hydrogen bonds between CC and AC, and CC and PEG to the shear strength for different PEG ratios. Because the PEG ratio is overall lower than the AC mass ratio, the contribution of hydrogen bonds between CC and PEG to the shear strength remains a small portion compared to the contribution of hydrogen bonds between CC and AC. When the PEG ratio increases, the contribution of hydrogen bonds between CC and AC reduces, while the contribution of hydrogen bonds between CC and PEG increases.

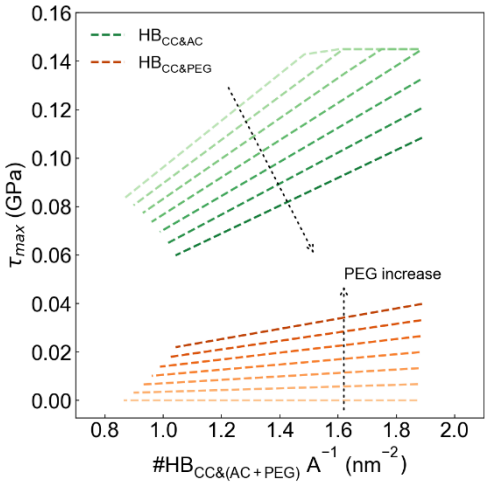

Figure 10. Shear strength contribution from hydrogen bonds between CC and AC, and hydrogen bonds between CC and PEG as determined by the shear strength model.

Table 1. The parameters for hydrogen bond model and shear strength model.

	HB model						**Shear strength model**		
Parameters	a_{AC} (nm^{-2})	b_{AC} (nm^{-2})	b_{PEG} (nm^{-2})	b_{MC}	c_{MC} (nm^{-2})	d_{MC}	α_{AC} (nN)	α_{PEG} (nN)	$\tau_{plateau}$ (GPa)
Values	1.87	2.48	2.54	2.57	4.2	5	0.096	0.052	0.145

Figure 11 compares the shear strength obtained from the shear strength model with MD shear strength data for different PEG ratios. The slope of the linear regression lines for all PEG ratios is very close to 1. Exception is the one for 25% PEG ratio, which has a value of 0.91. Remark that in Figure 8a we found a local minimum in shear strength at this location, which is neglected by the shear strength model proposed above. The shear strength model could be improved to consider this local effect. Figures 11a-g show that the shear strength data from the model fall into the 95% prediction interval. Figure 11h shows 74 out of 77 data points fall into the 95% prediction interval. These results of linear regression confirm the good agreement between model and MD data for all composites.

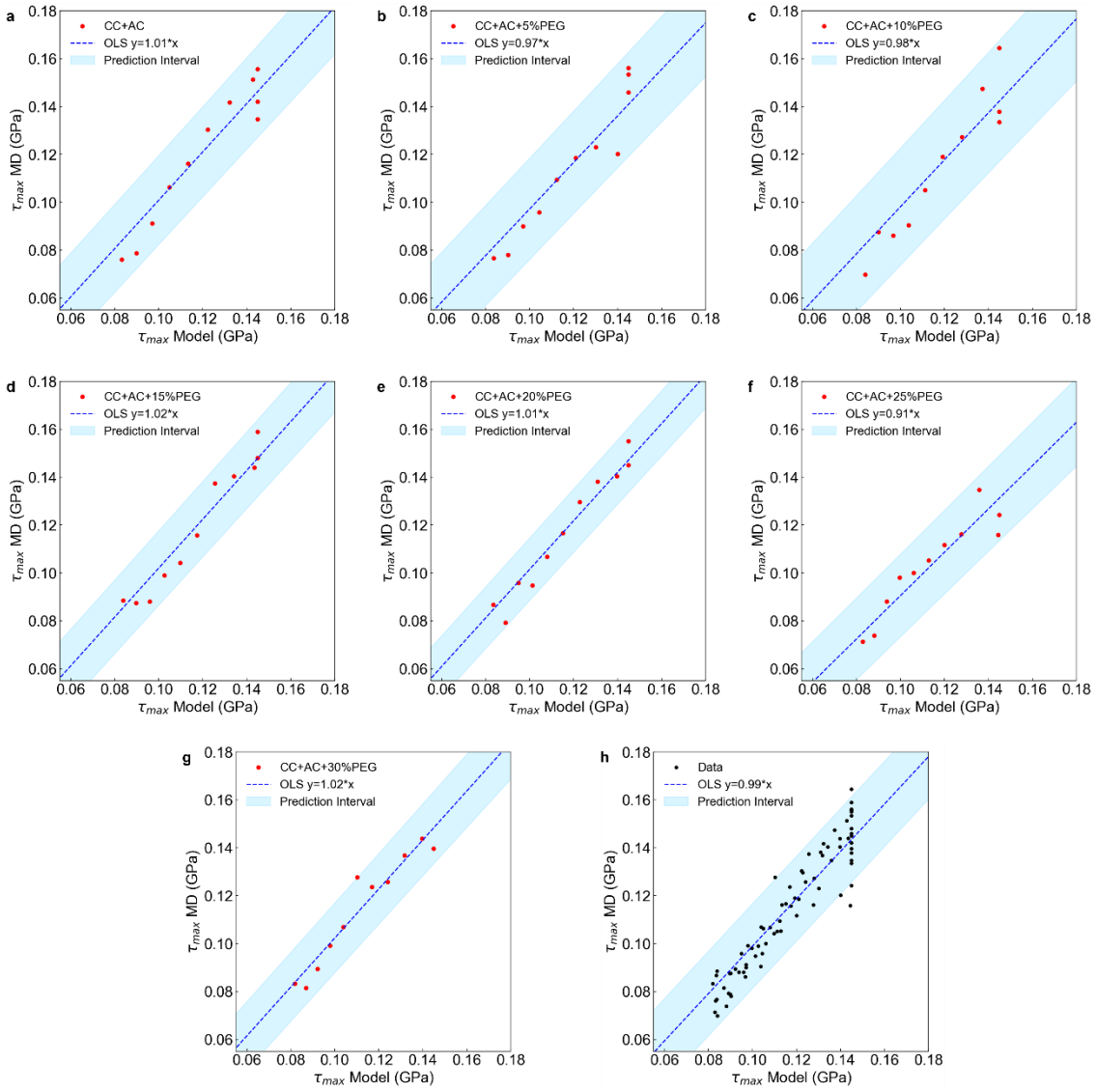

Figure 11. Shear strength obtained from shear strength model versus MD shear strength data for different PEG ratios: (a) 0%; (b) 5%; (c) 10%; (d) 15%; (e) 20%; (f) 25%; (g) 30%; (h) all PEG mixtures. The light blue shaded region depicts the 95% prediction interval.

5. Discussion

We remark that the shear strength provided by single hydrogen bond between CC and AC, and CC and PEG as determined in this study may depend on multiple factors, such as the specific force field utilized and simulation settings like pulling speed. The lower shear strength per hydrogen bond between CC and PEG than that between CC and AC might be dependent on parameters like charge assignment of the OPLS-AA force field. However, α_{AC} determined in this work, ~96 pN, agrees well with the estimated force rendered by single hydrogen bond between CC and galactoglucomannan matrix, ~140 pN, in our previous study with GROMOS

53a6 force field [9]. Although specific values may vary depending on the force field used, the conclusion that the force rendered by single hydrogen bond between CC and PEG is in the same order as that of CC and AC is believed to be general considering the good agreement between our current and previous studies.

Since it is difficult to realize the realistic structure of wood cell wall S2 layer of archaeological wood with highly degraded chemical structures in MD simulation, the observations in this study only apply to the simplified wood model used. Nevertheless, several important findings obtained with this simplified model still can provide insights to the understanding of the effect of PEG-treatment on fiber-reinforced composites. First, PEG-treatment does not have a significant impact on the hydrogen bond network at the interface between CC and matrix and thus also not on the shear strength. With increasing moisture content, the hydrogen bonds between (1) CC and AC and (2) CC and PEG are broken by water molecules leading to a decrease in shear strength. The number of hydrogen bonds broken between CC and matrix (AC+PEG) is nearly independent on PEG ratio and mainly determined by the moisture content. This means that a PEG treatment of AC has no negative effect on the shear strength. On the other side, we found in another study [31] that PEG reduces the moisture content at low relative humidity. Since the shear strength depends on the moisture content, the shear strength at low relative humidity (RH) will be less deteriorated by hydration. On the contrary, PEG treatment increases the moisture content at high relative humidity, leading to a deterioration of the shear strength and other mechanical properties. This means that PEG treated AC should be kept at low RH, as is done for archaeological wood in museums.

Second, the shear strength model proposed clearly shows that shear strength directly correlates with the number of interfacial hydrogen bonds and their strength. Third, at certain PEG ratio and low moisture content within a limited range due to the replacement of AC by PEG molecules, PEG-treatment can increase the hydrogen bond number between CC and matrix, which leads to slight enhancement of the shear force at the fiber-matrix interface.

6. Conclusions

This work characterizes the nanostructure and moisture-dependent interfacial mechanical properties of PEG-treated cellulose composites, consisting of a crystalline cellulose (CC) fiber and amorphous cellulose (AC) matrix using molecular dynamics simulations. It is found that the CC enriches the distribution of AC, PEG, and water molecules around the fiber-matrix interface. With increasing PEG ratios, PEG replaces AC around CC and forms a mixture with the AC matrix. With increasing moisture content, water molecules are found not only to be adsorbed by the AC matrix but also to fill the space between CC and matrix – therefore, influencing the interfacial mechanical properties. The shear stress versus displacement of CC

versus matrix manifests a stick-slip behavior during pullout. The hydrogen bond density between CC and matrix closely follows the stick-slip curve implying a strong correlation between shear stress and hydrogen bond network at the interface. The highest value of the maximum shear stress or shear strength appears at 3%-6% moisture content, which shows a slight enhancement of the interfacial mechanical property by cohesive forces exerted by the water molecules. A shear strength model based on the assumption that the shear stress results from the hydrogen bonds between the fiber and the matrix is developed and validated. It is found that PEG treated CC-AC composite maintains it shear strength and does not deteriorate the dependence of the shear strength on moisture content. The model reveals that the shear strength provided by per hydrogen bond between CC and PEG is lower than the shear strength provided per hydrogen bond between CC and AC. However, this lower value for PEG is partly compensated by an increase in the total number of hydrogen bonds between the matrix and CC. The competition between the strength and the number of hydrogen bonds results in a slight increase in shear stress in a limited range. This study improves the understanding of the fundamental mechanisms by which PEG-treatment influences the interfacial mechanical properties of the CC-AC composite at the molecular level. The methodology framework can be utilized to investigate the effect of PEG-treatment on the mechanical properties of wood S2 layer composite with realistic components and further on a composite with decayed structure in the archeological wood.

Acknowledgements

Acknowledgements. Add support from Canada chair and SNF project intoS2.

Appendix A. Supplementary Information

A.1. The parameters for PEG ratios and moisture contents

Table S1 The PEG ratio (m_{PEG}) and the moisture content (m) of all the composites analyzed.

	m_{PEG} (%)						
	0	5	10	15	20	25	30
m (%)	dry	dry	dry	dry	dry	dry	dry
	3.0	2.9	2.7	2.6	2.5	2.4	2.3
	6.0	5.7	5.5	5.2	5.0	4.8	4.6
	9.0	8.6	8.2	7.8	7.5	7.2	6.9
	12.0	11.4	10.9	10.4	10.0	9.6	9.2
	15.0	14.3	13.6	13.0	12.5	12.0	11.5
	18.0	17.1	16.4	15.7	15.0	14.4	13.8
	21.0	20.0	19.1	18.3	17.5	16.8	16.2
	24.0	22.8	21.8	20.9	20.0	19.2	18.5
	27.0	25.7	24.5	23.5	22.5	21.6	20.8
	30.0	28.6	27.3	26.1	25.0	24.0	23.1

A.2. Density prediction by rule of mixture (RoM)

The volume of each component can be determined from their mass and density:

$$V_{CC} = \frac{mass_{CC}}{\rho_{CC}} \quad (S1a)$$

$$V_{AC} = \frac{mass_{AC}}{\rho_{AC}} \quad (S1b)$$

$$V_{PEG} = \frac{mass_{PEG}}{\rho_{PEG}} \quad (S1c)$$

where $mass_{CC}$, $mass_{AC}$, $mass_{PEG}$ is the mass of CC, AC, and PEG, respectively, and ρ_{CC}, ρ_{AC} , ρ_{PEG} is the dry density of CC, AC, and PEG respectively. For the CC-AC-PEG composites, the $mass_{CC}$ and $mass_{AC}$ are constant, while $mass_{PEG}$ increases proportionally with PEG ratio. The density of each component in the composite is obtained from MD: ρ_{cc}= 1.6 g cm^{-3}, ρ_{AC}=1.4 g cm^{-3} and ρ_{PEG}=1.1 g cm^{-3}.

The total volume equals obtained by summing up the volumes of the three components then becomes:

$$V_{total} = V_{CC} + V_{AC} + V_{PEG} \quad (S2)$$

1. Classical RoM

Using the by classical Rule of Mixture (RoM), the density of the composite ρ_{com} equals:

$$\rho_{com} = \frac{V_{CC}}{V_{total}}\rho_{CC} + \frac{V_{AC}}{V_{total}}\rho_{AC} + \frac{V_{PEG}}{V_{total}}\rho_{PEG} \quad (S3)$$

Figure 2 shows that the density of the composite calculated by classical RoM (blue dashed line and points) underestimates the density of composite at all PEG ratios, except at zero PEG ratio.

2. New RoM

The volumetric PEG ratio β is defined as:

$$\beta = \frac{V_{PEG}}{V_{AC}} \quad (S4a)$$

which is related to the PEG mass ratio m_{PEG} as

$$\beta = \frac{V_{PEG}}{V_{AC}} = \frac{mass_{PEG}/\rho_{PEG}}{mass_{AC}/\rho_{AC}} = \frac{\rho_{AC}}{\rho_{PEG}}\frac{mass_{PEG}}{mass_{AC}} = \frac{\rho_{AC}}{\rho_{PEG}}m_{PEG} \quad (S4b)$$

In [31] it was shown that PEG fills the initial porosity of AC gradually at increasing PEG ratio. Due to the pore filling of AC by PEG, the current volume of the composite is lower than the total volume defined in Equation S2. The difference between total volume and the current volume equals the pore volume filled by PEG. The ratio of the volume of PEG, that fills the porosity of AC, and AC volume, is then:

$$\beta^{Fill} = \frac{V_{total} - V_{MD}}{V_{AC}} \quad (S5)$$

where V_{MD} is the volume of the entire composite at the equilibrium state obtained directly from the MD simulation. The ratio β^{Fill} can be interpreted as the part of the initial porosity of AC ϕ_{AC} filled with PEG. Denoting the current porosity of AC as ϕ and assuming that the change in porosity depends on the current porosity, the decrease in porosity $d\phi$ related to a change in β becomes*:*

$$d\phi = -b\phi d\beta \quad (S6)$$

Integration on both sides leads to:

$$\phi = \phi_{AC}\exp(-b\beta) \quad (S7)$$

The difference between the initial and current porosity equals:

$$\beta^{Fill} = \phi_{AC} - \phi_{AC}\exp(-b\beta) \quad (S8)$$

The initial porosity ϕ_{AC} of AC equals 0.05. The decay parameter b is obtained by fitting Equation S8 to data in Figure S1 showing β^{Fill} versus β. The parameters b equals 7.

The remaining volume of PEG that does not fill the porosity of AC by PEG equals:

$$V^*_{PEG} = (\beta - \beta^{Fill})V_{AC} \quad (S9)$$

The total volume of the composite is then:

$$V^*_{total} = V_{CC} + V_{AC} + V^*_{PEG} \quad (S10)$$

The density predicted by the new RoM taking into account pore filling by PEG then is:

$$\rho^*_{com} = \frac{V_{CC}}{V^*_{total}}\rho_{CC} + \frac{V_{AC}}{V^*_{total}}\rho_{AC} + \frac{V_{PEG}}{V^*_{total}}\rho_{PEG} \quad (S11)$$

Figure 2 shows a good agreement between the predicted density by the new RoM (the black dashed line and points) and the measured values from MD simulations.

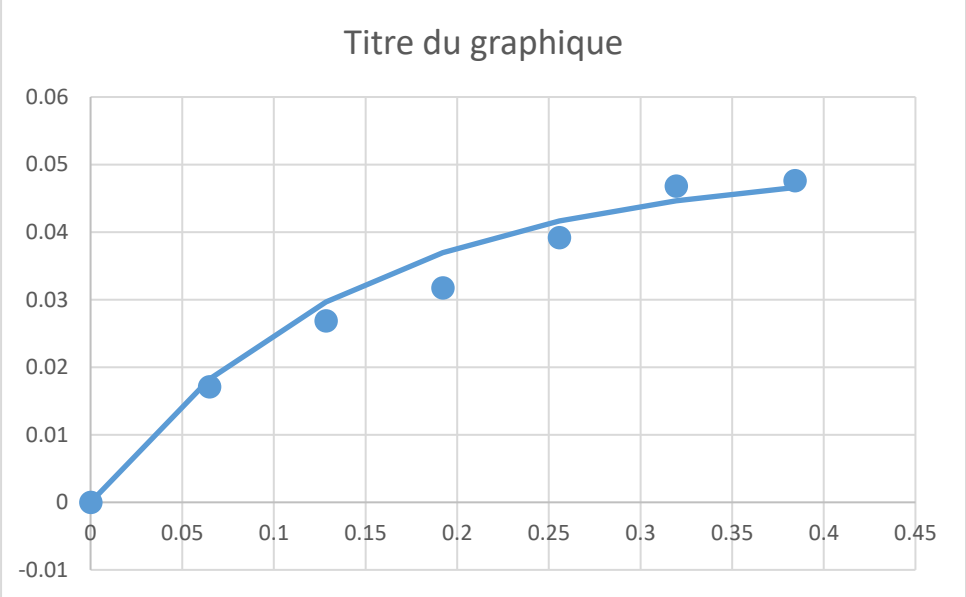

Figure S1. Volume ratio of PEG filling the porosity of AC versus PEG volume ratio. The solid curve shows the model prediction by Equation S8. Figure to be updated.

A.3. Stokes-Einstein radius of PEG

The Stokes-Einstein equation reads:

$$D = \frac{k_B T}{6\pi\eta r_s} \quad (S12)$$

where k_B is Boltzmann's constant, T the temperature, D the diffusion coefficient, η the viscosity and r_s the Stokes-Einstein radius of the molecule. Rearranging the equation, the radius becomes:

$$r_s = \frac{k_B T}{6\pi\eta D} \quad (S13)$$

The viscosity and self-diffusion coefficients of PEG200 molecule are determined in previous experimental studies at 300 K: $\eta = 52.3$ mPa·s and $D = 0.27 \times 10^{-10}$ m^2/s [32]. The Stokes-Einstein radius of PEG200 is then 1.56 Å.

Using the viscosity of water at 20 °C equal to 1.0019 mPa·s [33], and the self-diffusion coefficient of water at 25 °C $2.299 \cdot 10^{-9}$ $m^2 \cdot s^{-1}$ [34], the Stokes-Einstein radius of water molecule is equal to 0.955 Å.

A.4. Exponential decay of the number of hydrogen bond with moisture content

Figure 6a shows that the density of hydrogen bonds between CC and matrix decreases with increasing moisture content, but that the HB density is independent of the PEG ratio. The decrease in number of hydrogen bonds is related to the breakage of hydrogen bonds by water molecules. The number of HBs depends on the number of adsorbed water molecules N_W, or, $\#HB(N_W)$. When the number of adsorbed water molecules changes by dN_W, we can write:

$$\#HB(N_W + dN_W) = \#HB(N_W) - b_{N_W} \cdot \#HB(N_W) \cdot dN_W \quad \text{(S14)}$$

number also the equations below

where b_{N_W} is the exponential decay constant describing the rate of HB breaking per water molecule adsorbed. The equation can be rearranged to:

$$d\#HB(N_W)/\#HB(N_W) = -b_{N_W} \cdot dN_W$$

And solved by integration:

$$\#HB(N_W) = \#HB(dry) * \exp\left(-b_{N_W} \cdot N_W\right)$$

where $\#HB(dry)$ is the number of hydrogen bonds between CC and matrix at the dry state, i.e., $\#HB(dry) = \#HB(N_W = 0)$.

Considering that the moisture content is proportional to N_W, and the hydrogen bond number can be normalized by the contact surface area of CC and matrix, we find that

$$\#HB_{CC\&(AC+PEG)}\ A^{-1}(m_{PEG}, m) \sim \exp(-b_{MC} \cdot m)$$

which justifies the use of an exponential function in Equation 8.

A.5. Correlation between atom number density peak and hydrogen bond numbers

The relation shows the peak values of the atom number density of the matrix atoms are linearly correlated with the hydrogen bond numbers between the CC and matrix atoms, which demonstrates that the atom distribution and structure of the matrix near the CC surface are determined by the hydrogen bonds between CC and matrix. The peak position of the AC atoms, PEG atoms, and water atoms in Figure S2a and Figure S2b are mainly determined by the hydrogen bond formation of matrix atoms with CC.

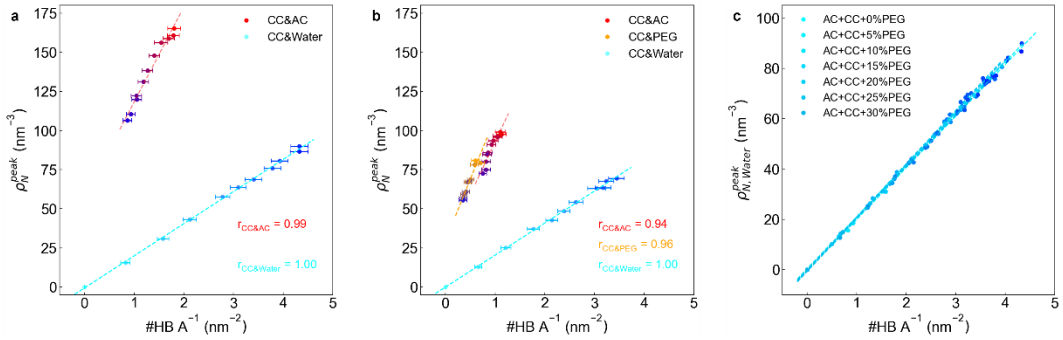

Figure S2. Peak in atom number density ρ_N^{peak} versus areal density of interfacial hydrogen bonds $\#HB\ A^{-1}$ (a) ρ_N^{peak} of AC and water atoms versus HB density between CC and AC, and CC and water from Figure 3a for the composite without PEG. (b) ρ_N^{peak} of AC, PEG, and water atoms versus HB density between CC and AC, CC and PEG, CC and water for the composite of 30% m_{PEG}. (c) ρ_N^{peak} water atoms versus HB density between CC and water for different PEG ratios.

A.6. Hydrogen bond numbers at the CC-matrix interface

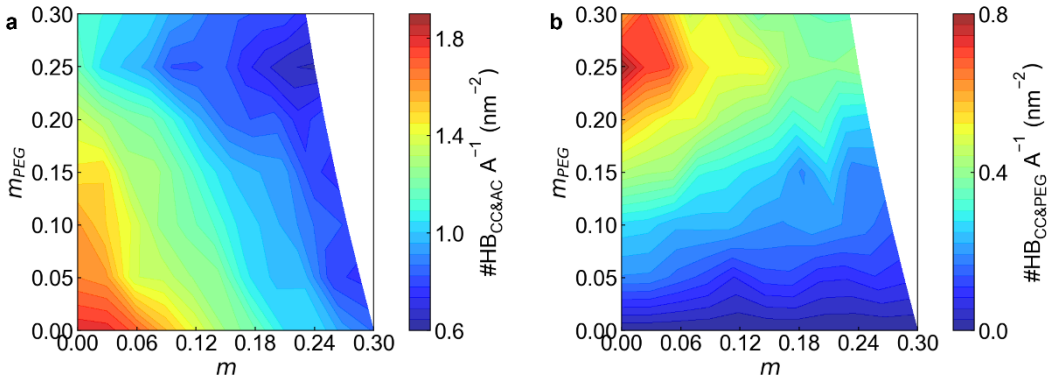

Figure S3. The two-dimensional contour view of the areal density of interfacial hydrogen bonds (a) between CC and AC and (b) between CC and PEG for all PEG ratios and moisture contents.

References

[1] J. Glausiusz, Wood — the vein that runs through human history, Nature 588 (2020) 26–27. https://doi.org/10.1038/d41586-020-03378-y.

[2] D. Derome, K. Kulasinski, C. Zhang, M. Chen, J. Carmeliet, Using Modeling to Understand the Hygromechanical and Hysteretic Behavior of the S2 Cell Wall Layer of Wood, in: A. Geitmann, J. Gril (Eds.), Plant Biomechanics: From Structure to Function at

Multiple Scales, Springer International Publishing, Cham, 2018: pp. 247–269. https://doi.org/10.1007/978-3-319-79099-2_12.
[3] C. Zhang, M. Chen, S. Keten, B. Coasne, D. Derome, J. Carmeliet, Hygromechanical mechanisms of wood cell wall revealed by molecular modeling and mixture rule analysis, Science Advances 7 (2021) eabi8919. https://doi.org/10.1126/sciadv.abi8919.
[4] A. Vorobyev, G. Almkvist, N.P. van Dijk, E.K. Gamstedt, Relations of density, polyethylene glycol treatment and moisture content with stiffness properties of Vasa oak samples, Holzforschung 71 (2017) 327–335. https://doi.org/10.1515/hf-2016-0202.
[5] E. Hocker, G. Almkvist, M. Sahlstedt, The Vasa experience with polyethylene glycol: A conservator's perspective, Journal of Cultural Heritage 13 (2012) S175–S182. https://doi.org/10.1016/j.culher.2012.01.017.
[6] M. Bardet, G. Gerbaud, C. Doan, M. Giffard, S. Hediger, G. De Paëpe, Q.-K. Trân, Dynamics property recovery of archaeological-wood fibers treated with polyethylene glycol demonstrated by high-resolution solid-state NMR, Cellulose 19 (2012) 1537–1545. https://doi.org/10.1007/s10570-012-9736-y.
[7] M. Broda, C.A.S. Hill, Conservation of Waterlogged Wood—Past, Present and Future Perspectives, Forests 12 (2021) 1193. https://doi.org/10.3390/f12091193.
[8] C. Hill, M. Altgen, L. Rautkari, Thermal modification of wood—a review: chemical changes and hygroscopicity, J Mater Sci 56 (2021) 6581–6614. https://doi.org/10.1007/s10853-020-05722-z.
[9] C. Zhang, M. Chen, B. Coasne, S. Keten, D. Derome, J. Carmeliet, Hygromechanics of softwood cellulosic nanocomposite with intermolecular interactions at fiber-matrix interface investigated with molecular dynamics, Composites Part B: Engineering 228 (2022) 109449. https://doi.org/10.1016/j.compositesb.2021.109449.
[10] M. Chen, B. Coasne, D. Derome, J. Carmeliet, Role of cellulose nanocrystals on hysteretic sorption and deformation of nanocomposites, Cellulose 27 (2020) 6945–6960. https://doi.org/10.1007/s10570-020-03247-x.
[11] M. Abraham, T. Murtola, R. Schulz, S. Páll, J.C. Smith, B. Hess, E. Lindahl, GROMACS: High performance molecular simulations through multi-level parallelism from laptops to supercomputers, (2015). https://doi.org/10.1016/J.SOFTX.2015.06.001.
[12] G. Bussi, D. Donadio, M. Parrinello, Canonical sampling through velocity rescaling, J. Chem. Phys. 126 (2007) 014101. https://doi.org/10.1063/1.2408420.
[13] M.J. Robertson, J. Tirado-Rives, W.L. Jorgensen, Improved peptide and protein torsional energetics with the OPLS-AA force field, J. Chem. Theory Comput. 11 (2015) 3499–3509. https://doi.org/10.1021/acs.jctc.5b00356.
[14] ERG Research Group, All-atom automatic OPLS-AA topology generator, (n.d.). http://erg.biophys.msu.ru/tpp/ (accessed March 22, 2023).
[15] D. Derome, C. Zhang, M. Chen, J. Carmeliet, Understanding swelling of wood through multiscale modeling, International Building Physics Conference (2018). https://surface.syr.edu/ibpc/2018/BE9/6.
[16] J. Li, H. Nawaz, J. Wu, J. Zhang, J. Wan, Q. Mi, J. Yu, J. Zhang, All-cellulose composites based on the self-reinforced effect, Composites Communications 9 (2018) 42–53. https://doi.org/10.1016/j.coco.2018.04.008.
[17] T.C.F. Gomes, M.S. Skaf, Cellulose-Builder: A toolkit for building crystalline structures of cellulose, Journal of Computational Chemistry 33 (2012) 1338–1346. https://doi.org/10.1002/jcc.22959.
[18] Y. Nishiyama, P. Langan, H. Chanzy, Crystal structure and hydrogen-bonding system in cellulose Iβ from synchrotron X-ray and neutron fiber diffraction, J. Am. Chem. Soc. 124 (2002) 9074–9082. https://doi.org/10.1021/ja0257319.
[19] S.-Y. Ding, S. Zhao, Y. Zeng, Size, shape, and arrangement of native cellulose fibrils in maize cell walls, Cellulose 21 (2014) 863–871. https://doi.org/10.1007/s10570-013-0147-5.
[20] J.D. Kubicki, H. Yang, D. Sawada, H. O'Neill, D. Oehme, D. Cosgrove, The shape of native plant cellulose microfibrils, Sci Rep 8 (2018) 13983. https://doi.org/10.1038/s41598-018-32211-w.

[21] B. Song, S. Zhao, W. Shen, C. Collings, S.-Y. Ding, Direct measurement of plant cellulose microfibril and bundles in native cell walls, Frontiers in Plant Science 11 (2020). https://www.frontiersin.org/articles/10.3389/fpls.2020.00479 (accessed January 19, 2023).
[22] Y. Habibi, L.A. Lucia, O.J. Rojas, Cellulose nanocrystals: chemistry, self-assembly, and applications, Chem. Rev. 110 (2010) 3479–3500. https://doi.org/10.1021/cr900339w.
[23] P. Virtanen, R. Gommers, T.E. Oliphant, M. Haberland, T. Reddy, D. Cournapeau, E. Burovski, P. Peterson, W. Weckesser, J. Bright, S.J. van der Walt, M. Brett, J. Wilson, K.J. Millman, N. Mayorov, A.R.J. Nelson, E. Jones, R. Kern, E. Larson, C.J. Carey, İ. Polat, Y. Feng, E.W. Moore, J. VanderPlas, D. Laxalde, J. Perktold, R. Cimrman, I. Henriksen, E.A. Quintero, C.R. Harris, A.M. Archibald, A.H. Ribeiro, F. Pedregosa, P. van Mulbregt, SciPy 1.0: fundamental algorithms for scientific computing in Python, Nat Methods 17 (2020) 261–272. https://doi.org/10.1038/s41592-019-0686-2.
[24] Z. Walsh, E.-R. Janeček, M. Jones, O.A. Scherman, Natural polymers as alternative consolidants for the preservation of waterlogged archaeological wood, Studies in Conservation 62 (2017) 173–183. https://doi.org/10.1179/2047058414Y.0000000149.
[25] L. Martínez, R. Andrade, E.G. Birgin, J.M. Martínez, PACKMOL: A package for building initial configurations for molecular dynamics simulations, Journal of Computational Chemistry 30 (2009) 2157–2164. https://doi.org/10.1002/jcc.21224.
[26] K. Kulasinski, S. Keten, S.V. Churakov, D. Derome, J. Carmeliet, A comparative molecular dynamics study of crystalline, paracrystalline and amorphous states of cellulose, Cellulose 21 (2014) 1103–1116. https://doi.org/10.1007/s10570-014-0213-7.
[27] S. Iwamoto, W. Kai, A. Isogai, T. Iwata, Elastic modulus of single cellulose microfibrils from tunicate measured by atomic force microscopy, Biomacromolecules 10 (2009) 2571–2576. https://doi.org/10.1021/bm900520n.
[28] R.R. Lahiji, X. Xu, R. Reifenberger, A. Raman, A. Rudie, R.J. Moon, Atomic force microscopy characterization of cellulose nanocrystals, Langmuir 26 (2010) 4480–4488. https://doi.org/10.1021/la903111j.
[29] A. Luzar, D. Chandler, Structure and hydrogen bond dynamics of water–dimethyl sulfoxide mixtures by computer simulations, The Journal of Chemical Physics 98 (1993) 8160–8173. https://doi.org/10.1063/1.464521.
[30] J. Teixeira, M.-C. Bellissent-Funel, Dynamics of water studied by neutron scattering, J. Phys.: Condens. Matter 2 (1990) SA105. https://doi.org/10.1088/0953-8984/2/S/011.
[31] A. Shomali, Molecular modeling of hygromechanical behavior of PEG-treated archeological wood S2 cell wall layer, Doctoral Thesis, ETH Zurich, 2024.
[32] M.M. Hoffmann, J.D. Kealy, T. Gutmann, G. Buntkowsky, Densities, viscosities, and self-diffusion coefficients of several polyethylene glycols, J. Chem. Eng. Data 67 (2022) 88–103. https://doi.org/10.1021/acs.jced.1c00759.
[33] J. Swindells, J. Coe Jr, T. Godfrey, Absolute Viscosity of Water at 20° C, Journal of Research of the National Bureau of Standard 48 (1952).
[34] M. Holz, S.R. Heil, A. Sacco, Temperature-dependent self-diffusion coefficients of water and six selected molecular liquids for calibration in accurate 1H NMR PFG measurements, Phys. Chem. Chem. Phys. 2 (2000) 4740–4742. https://doi.org/10.1039/B005319H.